Research Square

Preprints are preliminary reports that have not undergone peer review.
They should not be considered conclusive, used to inform clinical practice,
or referenced by the media as validated information.

Acceptance cone coupling and pixel size dependence in micro-LEDs with surface domes

Jung-Hun Choi

jhchoi@kicet.re.kr

Korea Institute of Ceramic Engineering and Technology

Ji-Hyeon Park

Korea Institute of Ceramic Engineering and Technology

Dae-Woo Jeon

Korea Institute of Ceramic Engineering and Technology

Article

Keywords: Micro-LED, Microdisplay, Light extraction, Far-field distribution, FDTD, Augmented reality

Posted Date: November 11th, 2026

DOI: https://doi.org/10.21203/rs.3.rs-11500299/v1

License: This work is licensed under a Creative Commons Attribution 4.0 International License.
Read Full License

Additional Declarations: No competing interests reported.

Acceptance cone coupling and pixel size dependence in micro-LEDs with surface domes

Abstract

Micro-LED-on-silicon (LEDoS) light engines require emission within the finite angular acceptance cone of the downstream collection optics in display systems. We use cylindrical finite-difference time-domain simulations to evaluate sidewall inclination and hemispherical surface domes using cone-coupled efficiency. The reference pixel has a 2.0 μm active diameter and a 4.0 μm pitch, with a representative collection half-angle of 15°. Extraction through the pixel-cell area and cone-coupled efficiency favor different structures. A low-index dome improves angular coupling, but increasing the sidewall angle beyond approximately 30° provides limited additional angular benefit while increasing the minimum pitch required for mesa non-overlap. The dome response is non-monotonic with refractive index. In the size sweep, the angular benefit becomes negligible at an active diameter of 1 μm, although a small extraction-related efficiency gain remains. These results connect pixel-level optical design to the collection requirements and geometric constraints of LEDoS light engines, within the tested dome geometry and source conditions.

Keywords: Micro-LED · Microdisplay · Light extraction · Far-field distribution · FDTD · Augmented reality

1 Introduction

Micro-LEDs are candidate light sources for augmented-reality microdisplays because of their brightness, contrast and lifetime [1–3]. For micro-LED-on-silicon (LEDoS) light engines, pixel emission must be collected and delivered through downstream optics. Projection optics and waveguide in-couplers accept only a finite angular range [4–7]. Increasing the total light extracted from a pixel therefore does not necessarily increase the optical power available to the engine. Pixel design must account for the fraction of source power entering the intended acceptance cone.

Previous studies have investigated inclined sidewalls and pixel geometry for light extraction [8, 9], size-dependent emission and recombination [10, 11], and photonic crystals or collimating structures for directional emission [12–15]. These approaches establish the importance of both extraction and emission directionality. For LEDoS-oriented design, the relevant question is how a surface dome and the underlying sidewall geometry jointly affect collection within a specified cone, while satisfying pixel-spacing constraints. A related question is whether a dome that benefits a larger pixel retains its angular advantage as the active diameter is reduced. These questions link pixel-level optical performance to the collection and scaling requirements of the light engine.

Here we compare extraction through the pixel-cell area with acceptance-cone coupling in a cylindrical finite-difference time-domain (FDTD) model. We evaluate the combined effects of sidewall inclination and a hemispherical dome, relate angular coupling to the minimum pitch for mesa non-overlap, and examine dome refractive index and pixel-size dependence. An Airy reference provides context for aperture scaling. The contribution is a joint assessment of collection performance and geometric constraints for LEDoS-oriented pixel design; the model evaluates a representative collection cone rather than the transmission of a complete optical engine.

2 Model and metrics

2.1 Device and collection geometry

The reference pixel has active diameter $d = 2.0$ μm and pitch $p = 4.0$ μm, using the pitch reported for a microdisplay backplane [14]. Its vertical stack follows the resonant-cavity design of Vögl et al. [9] and consists of n-GaN, a mesa containing the multiple quantum wells (MQWs), indium tin oxide (ITO), SiO_2 and an Ag reflector. The layer thicknesses are 1.5, 0.6, 0.05 and 0.15 μm, respectively, above the reflector. The MQW plane lies 0.095 μm above the ITO interface. The vertical stack is fixed across the sweeps.

Figure 1 distinguishes the active diameter from the dome aperture and the two collection measures. The sidewall angle α is measured from the vertical. The reference dome has aperture radius $a = p/2 = 2.0$ μm, sag $h = a$ and refractive index $n = 1.46$, with direct contact to the n-GaN surface. The n-GaN and mirror terminate at the pixel-cell radius. Power crossing a top monitor within this pixel-cell area is counted separately from power radiated into the upper far-field hemisphere. Lateral leakage is not an explicit calculation of neighbor-pixel

crosstalk. The SiO_2 layer covers the mesa sidewalls and the underside of n-GaN, with Ag filling the surrounding region below the mesa top.

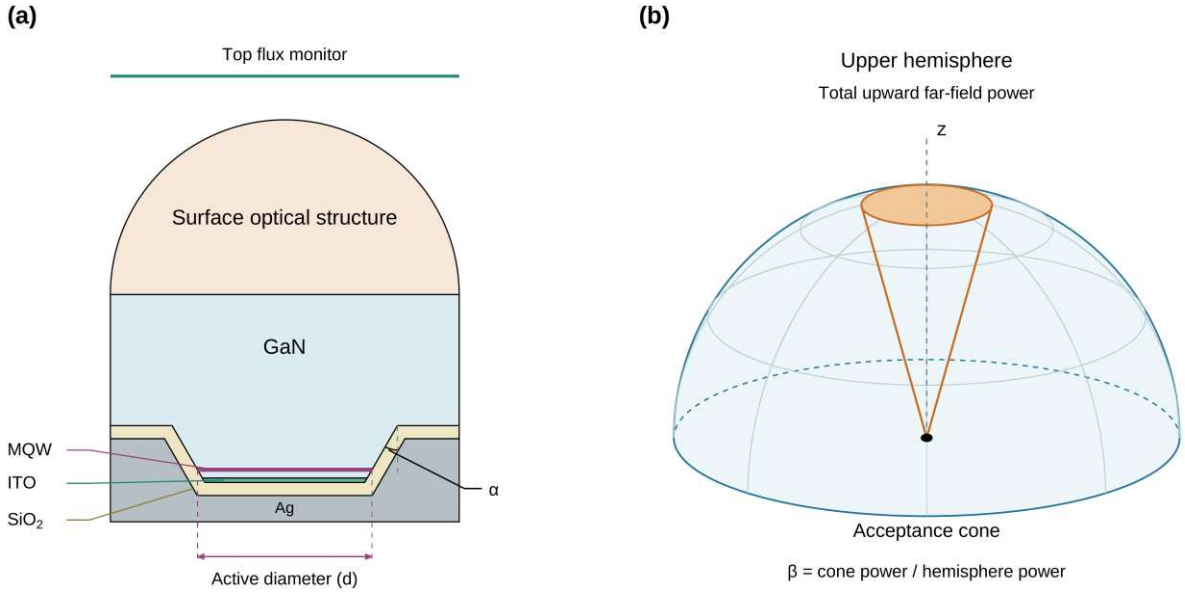


Fig. 1 Pixel structure and collection geometry. (a) Cross-section at α = 30°, showing the multiple-quantum-well (MQW) plane, material layers and top flux monitor; the surface optical structure is illustrated by a hemispherical dome and d denotes the active diameter. (b) Upper far-field hemisphere and acceptance cone, where β is the fraction of hemispherical power within the cone

2.2 Optical metrics

Let P_{src} denote the power radiated by the source in the structure and P_{top} the power crossing the top monitor of radius p/2. Extraction through the pixel-cell area is $\eta_{planar,cell} = P_{top}/P_{src}$. Hemispherical extraction η_{hemi} is the upper-hemisphere far-field power divided by P_{src}, obtained by a near-to-far-field transform. The fraction of upper-hemisphere power inside the acceptance cone is

$$\beta(\theta_{acc}) = \frac{P(\theta \le \theta_{acc})}{P(\theta \le 90°)} \quad (1)$$

The cone-coupled efficiency and the angular gain relative to a Lambertian distribution are

$$\eta_{eff}(\theta_{acc}) = \eta_{hemi} \times \beta(\theta_{acc}) \quad (2)$$

$$D(\theta_{acc}) = \frac{\beta(\theta_{acc})}{sin^2\,\theta_{acc}} \quad (3)$$

The collection half-angle θ_{acc} is set to 15° as a representative optical acceptance condition. Cone-coupled efficiency η_{eff} is the primary objective; β measures angular redistribution, and D is the angular gain relative to a Lambertian emitter. β and the efficiencies are reported in percent, and differences between configurations, such as Δβ, are absolute differences. These optical metrics exclude internal quantum efficiency and downstream optical losses.

2.3 Numerical method and checks

Simulations use Meep [16] in cylindrical coordinates [17]. Emission is represented by an incoherent, area-weighted dipole ensemble over the active region [9, 18, 19]. The principal quantitative sweeps use 20 radial positions and two source orientations, combined using the reported 1:1 transverse-electric (TE) to transverse-magnetic (TM) convention and 2πr radial weighting. The radial spacing is 50 nm for the 2.0 µm reference diameter; it is not assumed fixed across the size sweep. In-plane emission is represented by an E_r source without a separately simulated E_φ source; the campaign uses the 1:1 source combination stated above. This approximation was assessed in the isolated-device benchmark but not re-evaluated for the dome geometries.

The emission spectrum is Gaussian with a 30 nm full width at half maximum centered at 460 nm, sampled at 51 frequencies over 409–511 nm and applied as a spectral weight. The broader FDTD source pulse uses fwidth = 0.2/λ. The reference resolution is 80 pixels per µm and the Courant factor is 0.3. The computational cell and near-to-far surface radii are 7.25 and 6.0 µm, respectively. The maximum run time is 4000 simulation time

units, with a decay tolerance of 0.0001 checked every 50 periods. Baseline GaN, ITO and SiO_2 indices are 2.45, 2.00 and 1.46; Ag uses a Drude model compared with Johnson and Christy [20]. The refractive-index scan uses literature material parameters [21–23], namely GaN 2.4764, ITO 1.9557 + 0.00729i and SiO_2 1.4648, with the same Ag model.

For the unstructured pixel, changing the ensemble from 8 to 20 positions changes β by at most 0.1 %. Changing resolution from 80 to 60 pixels per µm changes the dome-gain ratio by a relative 2.25 %. A comparison tolerance of $\Delta\beta = 0.7$ % is used to interpret the sidewall plateau and the small-pixel dome gain; it is not a statistical confidence interval or an uncertainty estimate for η_{eff}. At the isolated-device benchmark, the 1:1-weighted extraction efficiencies are 43.9 % and 55.2 % at $\alpha = 0°$ and 30°, compared with the literature simulation values 44 % and 57 % [9]. This is trend reproduction against a simulation reference, not an experimental comparison.

Angular profiles are sampled from 0° to 90° in 0.5° steps. Relative angular intensity is obtained by removing the $\sin\theta$ angular weighting from the power-per-angle profile and normalizing each curve to its maximum; the axial value ($\theta = 0°$), where this ratio is undefined, is obtained from an even-symmetry quadratic fit to the three nearest samples. The displayed negative-angle branch mirrors the axisymmetric solution. Cone fractions are integrated from the original power-per-angle profiles, not from the area enclosed by the polar curves.

For the field maps, the incoherently weighted squared Er and Ez components are summed before the square root is taken, and Eφ is excluded. All three panels share one linear color scale, which saturates at most the brightest 0.5 % of pixels in $z \geq 1.5$ µm. The computed domain ($r \geq 0$) is mirrored about the axis. The maps are shown for the reference conditions at $\alpha = 40°$, 460 nm and a top-gap parameter of 2.5 µm, whereas the collection metrics are spectrally weighted.

3 Results and discussion

3.1 Extraction and acceptance-cone coupling

Table 1 shows that extraction through the pixel-cell area and cone-coupled efficiency favor different structures. The high-index dome on the vertical-sidewall mesa has the highest $\eta_{planar,cell}$ of all configurations but the lowest η_{eff} among the dome configurations. Conversely, the low-index dome at $\alpha = 40°$ provides the highest η_{eff} in this comparison. Collection within the intended acceptance cone is therefore necessary when comparing pixel structures for LEDoS optics.

Table 1 Extraction through the pixel-cell area and cone-coupled efficiency for the reference pixel under baseline material conditions. AR denotes an anti-reflection coating; $\theta_{acc} = 15°$

Configuration	$\eta_{planar,cell}$ (%)	$\eta_{eff}(15°)$ (%)
$\alpha = 0°$, bare	33.8	13.2
$\alpha = 0°$, dome n = 1.46	50.3	20.8
$\alpha = 0°$, dome n = 2.50	64.7	17.2
$\alpha = 40°$, bare	34.1	14.7
$\alpha = 40°$, dome n = 1.46	50.9	24.5
$\alpha = 40°$, dome n = 2.50	56.7	18.3
$\alpha = 40°$, dome n = 2.50 + AR	61.5	19.2

Figure 2 connects emission directionality with collection at $\alpha = 40°$. Panel (a) compares angular-intensity shapes, while panels (b) and (c) quantify angular-bin power and efficiency. Each curve in (a) is normalized to its own maximum, so peak heights do not compare absolute output. The low-index hemisphere increases β from 21.1 % to 33.4 % and η_{eff} from 14.7 % to 24.5 %. Its median emission angle is 21.3°, compared with 29.5° for the bare pixel. The high-index dome is intermediate, with a median angle of 24.5°. Between the low- and high-index domes, extraction through the pixel-cell area increases but η_{hemi} decreases from 73.3 % to 70.0 %. The corresponding angular gain relative to a Lambertian distribution, D(15°), increases from 3.14 for the

bare pixel to 4.98 for the low-index hemisphere. The reference comparisons use d = 2.0 µm, p = 4.0 µm, dome h = a = 2.0 µm and baseline materials.

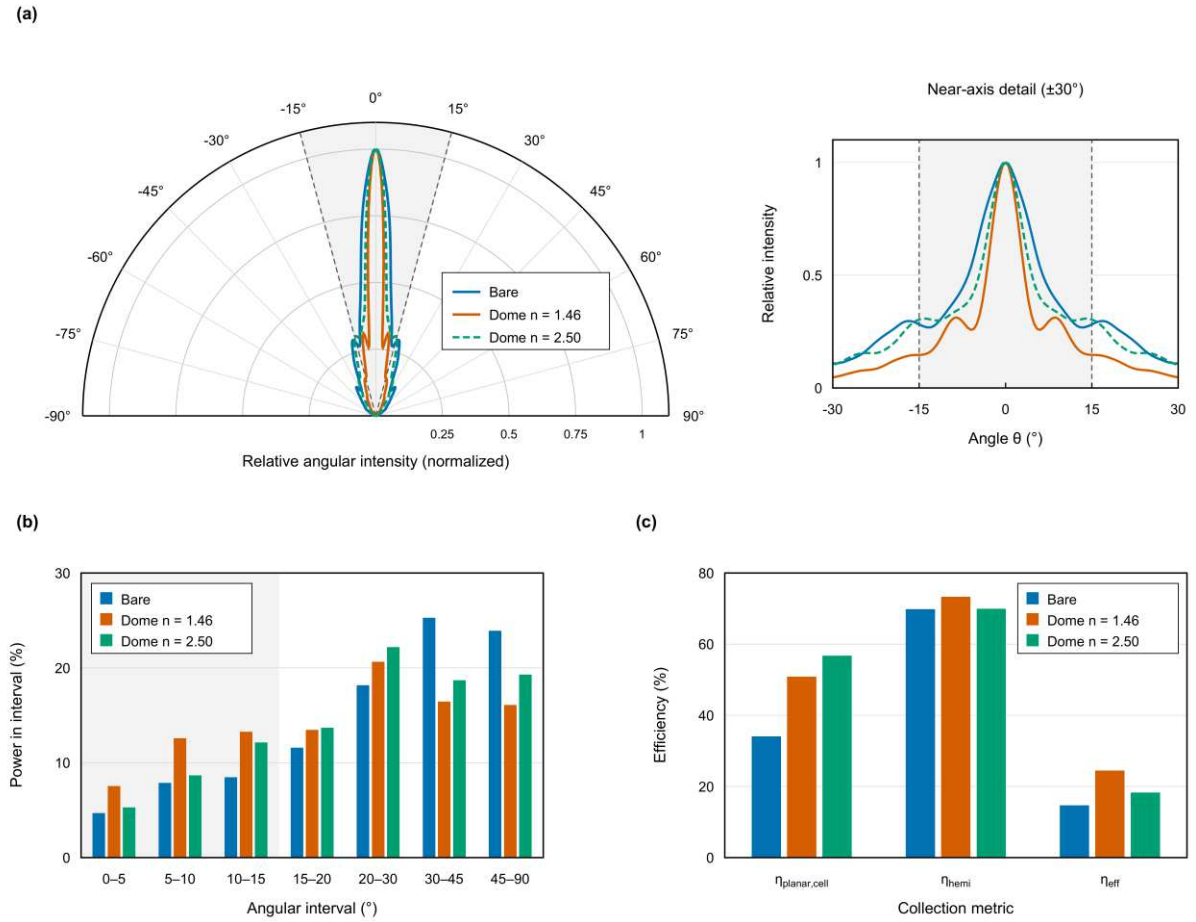


Fig. 2 Angular emission and collection at α = 40°. (a) Angular intensity normalized to each maximum and mirrored about the axis (the inset shows the same data within ±30°, and dashed lines mark the ±15° cone). (b) Power in each angular interval as a percentage of upper-hemisphere power, with the 0–15° cone shaded. (c) Extraction and collection efficiencies as percentages of source power

A ray emitted from the center of a sphere meets its surface normally, providing a geometric interpretation of the hemisphere. Here, the MQW ensemble lies below that center and is spatially extended; the construction therefore does not establish the absence of total internal reflection (TIR). The calculated angular distribution and collection efficiency support improved angular outcoupling by the low-index dome.

The field maps in Fig. 3 show axial field concentration above the low-index dome and pronounced internal structure in the high-index dome. They provide spatial context for the collection results, while the far-field metrics in Fig. 2 quantify angular coupling. Map brightness represents the displayed field components under common excitation, rather than extraction efficiency.

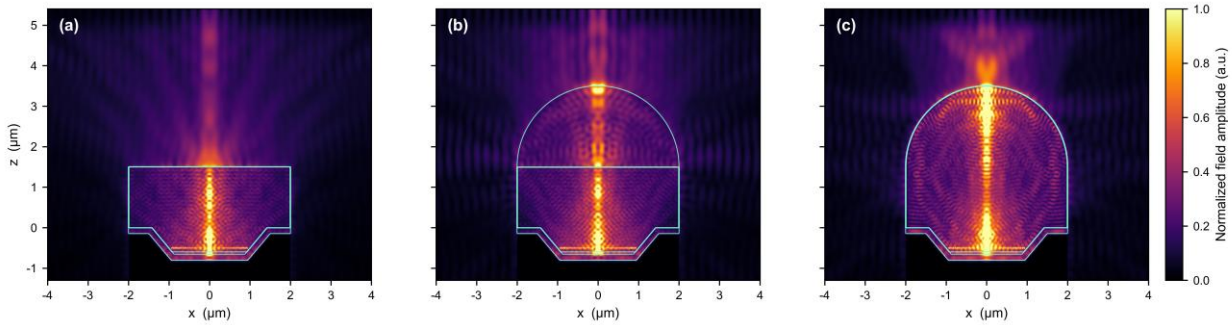


Fig. 3 Field distributions at 460 nm for (a) the bare pixel and domes with (b) n = 1.46 and (c) n = 2.50, at α = 40°. Color shows the field amplitude normalized to a scale common to all panels, and material interfaces are outlined

3.2 Sidewall inclination and minimum pixel pitch

Figure 4 compares sidewall-angle dependence under identical numerical settings. The bare pixel reaches its sampled maximum β at α = 20°. With the low-index dome, the 30°, 35° and 40° values lie within the adopted tolerance (Δβ = 0.7 %) of the dome maximum; only the sampled 20° bare-pixel point meets the same criterion for the bare pixel. Thus, increasing the sidewall inclination beyond approximately 30° provides limited additional angular benefit with the dome. The highest sampled η_{eff} is 24.9 % at 30°, supporting this angle as a design point without identifying a unique best angle from β. This sweep uses the reference geometry, n = 1.46, baseline materials and a top-gap parameter of 2.5 µm.

The dome gain in β increases from 8.4 % at α = 0° to 12.3 % at 40°, giving an interaction term of 3.9 %. Sidewall inclination and dome addition are thus super-additive in this metric between the specified endpoints. The result establishes that their angular effects are not independent; a possible interpretation is that the dome modifies the escape of light already redirected by the sidewall.

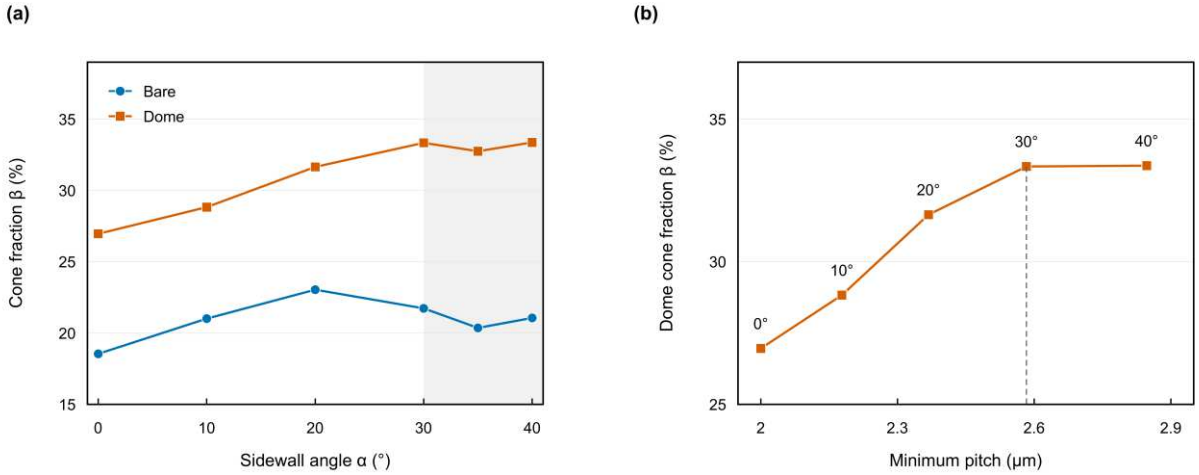


Fig. 4 Sidewall inclination and minimum pitch. (a) Cone fraction of bare and dome pixels; shading marks the sampled 30°–40° region of limited β variation. (b) Dome β, computed at p = 4.0 µm, against the minimum pitch for mesa non-overlap, labeled by sidewall angle, with the dashed line at 30°

The sidewall also imposes a geometric pitch constraint,

$$p_{min} = 2R_{mesa,top} = 2(d/2 + h_{MQW}\tan\alpha) \quad (4)$$

Here $R_{mesa,top}$ is the radius of the mesa top, h_{MQW} = 0.505 µm is the distance from the multiple-quantum-well plane to the mesa top, and p_{min} is the minimum pitch for mesa non-overlap. At d = 2 µm, p_{min} increases from 2.583 µm at 30° to 2.847 µm at 40°. Approximately 30° therefore combines the observed angular benefit with a smaller required pixel spacing. Fabrication and electrical-isolation margins must be added separately.

3.3 Dome refractive index

The index scan in Fig. 5 uses α = 30° and the literature material set; its values are not directly compared with the α = 40° baseline-material values in Fig. 2. β decreases from 33.7 % at n = 1.46 to 12.7 % at n = 1.80, then recovers to 26.6 % at n = 2.50. Figure 5a shows the resulting non-monotonic cone-coupled efficiency, while Fig. 5b separates angular coupling from hemispherical extraction. Two trends are apparent in the angular-power distribution. At intermediate indices, the 0°–10° fraction falls while the 20°–30° fraction rises, with relatively little change in η_{hemi}. This is consistent with redistribution outside the acceptance cone. At n = 2.50, η_{hemi} decreases to 64.4 %, consistent with reduced escape from the higher-index dome. These observations support distinct redistribution and escape-loss contributions without quantifying their individual causal shares. The reference dimensions and ensemble are retained, with a top-gap parameter of 2.5 µm.

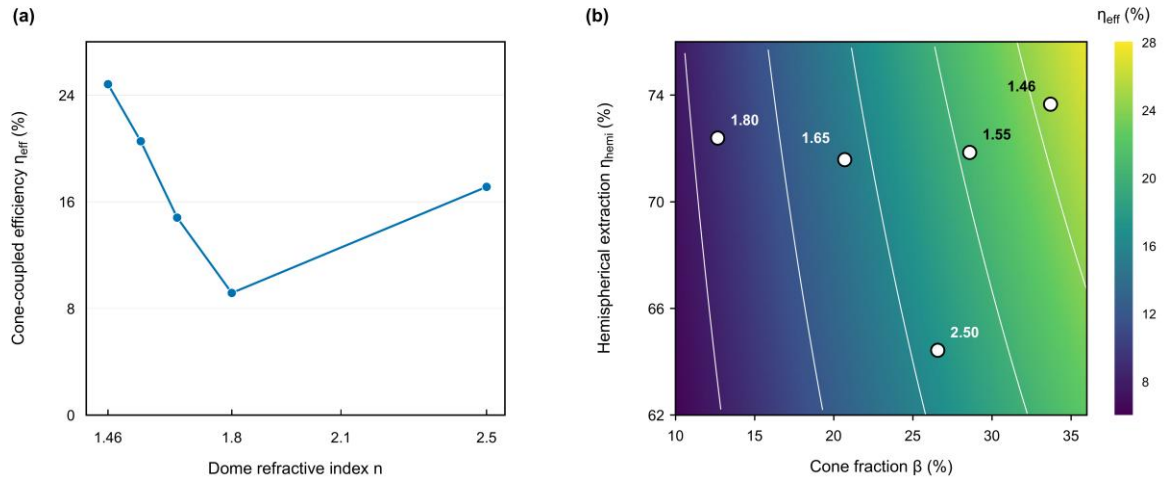


Fig. 5 Refractive-index dependence at α = 30° using the literature material set. (a) Cone-coupled efficiency. (b) The same simulated conditions in the β–η_{hemi} plane, labeled by refractive index; the background shows $\eta_{eff} = \beta \times \eta_{hemi}$

The sampled points do not locate the boundaries of an entire unfavorable index interval. Raising n from 1.46 to 1.55 reduces η_{eff} from 24.8 % to 20.5 %, a relative reduction of 17.2 %, under the same conditions. This comparison supports material selection within the tested conditions.

The separate baseline-material comparison explains why index matching alone is insufficient. At α = 40°, increasing n from 1.46 to 2.50 increases $\eta_{planar,cell}$ while reducing β and η_{eff}. The dome/air critical angle changes from 43.2° to 23.6°. A quarter-wave SiO_2 coating increases extraction through the pixel-cell area, but its Δβ of 0.7 % is only at the adopted tolerance, and it does not recover the low-index dome's cone-coupled efficiency. Across α = 0° and 40°, the pixel-cell extraction gain from index matching decreases from 14.4 % to 5.8 %, in contrast to the super-additive behavior of β in Sect. 3.2.

3.4 Pixel-size dependence of the dome benefit

Figure 6 compares bare and hemispherical-dome pixels at d = 1, 2 and 3 μm with α = 30°, p = 2d and h = a. This sweep uses baseline materials and a top-gap parameter of 3.6 μm rather than the 2.5 μm of the reference geometry, so its values are compared only within the sweep.

The dome increases β by 11.1 % at d = 2 μm and 8.5 % at d = 3 μm, but by only 0.05 % at d = 1 μm, a negligible change below the adopted comparison tolerance. Cone-coupled efficiency reaches 1.040 times the bare-pixel value at d = 1 μm, compared with 1.650 and 1.505 times at the larger diameters. Since $\eta_{eff} = \eta_{hemi} \times \beta$, the remaining gain at d = 1 μm is primarily associated with hemispherical extraction. The β tolerance does not establish the significance of the small η_{eff} change.

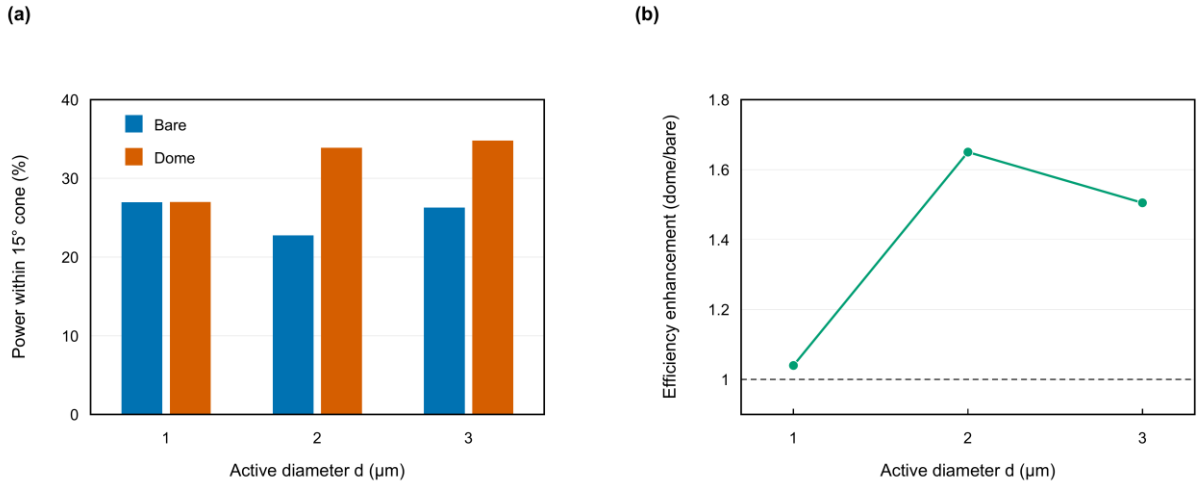


Fig. 6 Pixel-size dependence at α = 30°, with p = 2d and h = a. (a) Percentage of upper-hemisphere power within the 15° cone for bare and dome pixels. (b) Dome-to-bare ratio of cone-coupled efficiency, with the dashed line at unity

A uniformly illuminated circular aperture provides a simple reference for the effect of aperture size [24]. For an aperture diameter equal to d, the Airy fraction within 15° decreases from 83.7 % at d = 2 μm to 53.4 % at d = 1 μm. This illustrates the collection penalty of a smaller aperture. However, the dome aperture is larger than the active diameter, so the reference does not establish a universal pixel-size limit. The direct FDTD result is that the tested dome provides negligible angular improvement at d = 1 μm, while retaining gains at the larger sampled diameters.

The model is axisymmetric and treats a single pixel with smooth interfaces, a dome in direct contact with GaN and a blue source band centered at 460 nm. Current spreading, internal quantum efficiency, sidewall recombination and process variations are not included, so the optical metrics are not directly comparable with measured external quantum efficiencies [10, 11, 25–27]. Including dielectric absorption through the literature material set changes the dome-to-bare ratios in β and η_{eff} by about 2 % in relative terms. Square pixels, interacting arrays and experimental validation of the dome geometry remain for future work.

4 Conclusion

For LEDoS-oriented pixel design, collection within the intended optical acceptance cone can favor different structures from extraction through the pixel-cell area. A low-index hemispherical dome improves angular coupling in conjunction with sidewall inclination. Approximately 30° provides a design point with limited additional β benefit at larger angles and a smaller minimum-pitch requirement. Dome refractive index produces a non-monotonic response. The direct FDTD results also establish a size-dependent limit to the angular benefit of the tested dome, with negligible β improvement at 1 μm and retained gains at 2 and 3 μm. These sampled sizes do not locate a precise transition or a universal lower bound. The results support joint selection of pixel geometry and dome material according to the collection requirements of the optical engine.

Data availability. The simulation outputs underlying the figures and tables are available from the authors on reasonable request.

References

1. Y. Huang, E.-L. Hsiang, M.-Y. Deng, S.-T. Wu, Mini-LED, micro-LED and OLED displays: present status and future perspectives. Light Sci. Appl. 9, 105 (2020). https://doi.org/10.1038/s41377-020-0341-9
2. J. Xiong, E.-L. Hsiang, Z. He, T. Zhan, S.-T. Wu, Augmented reality and virtual reality displays: emerging technologies and future perspectives. Light Sci. Appl. 10, 216 (2021). https://doi.org/10.1038/s41377-021-00658-8
3. P.J. Parbrook, B. Corbett, J. Han, T.-Y. Seong, H. Amano, Micro-light emitting diode: from chips to applications. Laser Photonics Rev. 15, 2000133 (2021). https://doi.org/10.1002/lpor.202000133
4. B.C. Kress, I. Chatterjee, Waveguide combiners for mixed reality headsets: a nanophotonics design perspective. Nanophotonics 10, 41–74 (2021). https://doi.org/10.1515/nanoph-2020-0410
5. Y. Ding, Q. Yang, Y. Li, Z. Yang, Z. Wang, H. Liang, S.-T. Wu, Waveguide-based augmented reality displays: perspectives and challenges. eLight 3, 24 (2023). https://doi.org/10.1186/s43593-023-00057-z
6. Y. Qian, Z. Yang, S.-C. Chen, Y. Ma, Y.-C. Chen, H.-S. Chen, C.-L. Lin, S.-T. Wu, Power consumption of light engines for emerging augmented reality glasses: perspectives and challenges. Adv. Photonics 7, 034001 (2025). https://doi.org/10.1117/1.AP.7.3.034001
7. W. Han, C.-H. Song, B. Chun, D. Lee, J.-H. Park, J. Kwak, J.Y. Lee, Review of recent display advancements: augmented reality, virtual reality, quantum-dot light-emitting diodes and organic light-emitting diodes. J. Inf. Disp. 27, 15 (2026). https://doi.org/10.1007/s44469-026-00016-7
8. H.-Y. Ryu, J. Pyo, H.Y. Ryu, Light extraction efficiency of GaN-based micro-scale light-emitting diodes investigated using finite-difference time-domain simulation. IEEE Photonics J. 12, 1600110 (2020). https://doi.org/10.1109/JPHOT.2020.2977401
9. F. Vögl, A. Avramescu, F. Knorr, A. Lex, A. Waag, M. Hetzl, N. von Malm, Role of pixel design and emission wavelength on the light extraction of nitride-based micro-LEDs. Opt. Express 31, 22997 (2023). https://doi.org/10.1364/OE.489110
10. F. Vögl, A. Avramescu, S. Gelfert, A. Lex, A. Waag, M. Hetzl, N. von Malm, Optical characteristics of thin film-based InGaN micro-LED arrays: a study on size effect and far field behavior. Opt. Express 32, 17644 (2024). https://doi.org/10.1364/OE.523274
11. J.-H. Park, M. Pristovsek, W. Cai, H. Cheong, C.-M. Kang, D.-S. Lee, T.-Y. Seong, H. Amano, Dislocation suppresses sidewall-surface recombination of micro-LEDs. Laser Photonics Rev. 17, 2300199 (2023). https://doi.org/10.1002/lpor.202300199
12. M. Liu, X. Zheng, Improving the light extraction efficiency of GaN-based thin-film flip-chip micro-LEDs through inclined sidewall and photonic crystals. Electronics 13, 3750 (2024). https://doi.org/10.3390/electronics13183750

13. A. Luce, R. Alaee, A. Abass, Ultra-directional and high-efficiency μLEDs via gradient index filled micro-horn collimators. Sci. Rep. 16, 7391 (2026). https://doi.org/10.1038/s41598-026-39920-7

14. Q. Li, W. Tan, Y. Zhu, J. Guo, X. Jiang, 11-1: Invited paper: MicroLED displays for augmented reality smart glasses. SID Symp. Dig. Tech. Pap. 55, 104–107 (2024). https://doi.org/10.1002/sdtp.17464

15. E. Chen, Z. Yao, Z. Fan, W. Lai, T. Liang, Q. Yan, T. Guo, C.P. Chen, Collimated LED array with mushroom-cap encapsulation for near-eye display projection engine. IEEE J. Sel. Top. Quantum Electron. 30, 2000410 (2024). https://doi.org/10.1109/JSTQE.2024.3375929

16. A.F. Oskooi, D. Roundy, M. Ibanescu, P. Bermel, J.D. Joannopoulos, S.G. Johnson, Meep: a flexible free-software package for electromagnetic simulations by the FDTD method. Comput. Phys. Commun. 181, 687–702 (2010). https://doi.org/10.1016/j.cpc.2009.11.008

17. A. Taflove, S.C. Hagness, Computational Electrodynamics: The Finite-Difference Time-Domain Method, 3rd edn. (Artech House, Norwood, 2005)

18. C. Wiesmann, K. Bergenek, N. Linder, U.T. Schwarz, Photonic crystal LEDs: designing light extraction. Laser Photonics Rev. 3, 262–286 (2009). https://doi.org/10.1002/lpor.200810053

19. A. David, H. Benisty, C. Weisbuch, Photonic crystal light-emitting sources. Rep. Prog. Phys. 75, 126501 (2012). https://doi.org/10.1088/0034-4885/75/12/126501

20. P.B. Johnson, R.W. Christy, Optical constants of the noble metals. Phys. Rev. B 6, 4370–4379 (1972). https://doi.org/10.1103/PhysRevB.6.4370

21. A.S. Barker Jr., M. Ilegems, Infrared lattice vibrations and free-electron dispersion in GaN. Phys. Rev. B 7, 743–750 (1973). https://doi.org/10.1103/PhysRevB.7.743

22. T.A.F. König, P.A. Ledin, J. Kerszulis, M.A. Mahmoud, M.A. El-Sayed, J.R. Reynolds, V.V. Tsukruk, Electrically tunable plasmonic behavior of nanocube–polymer nanomaterials induced by a redox-active electrochromic polymer. ACS Nano 8, 6182–6192 (2014). https://doi.org/10.1021/nn501601e

23. I.H. Malitson, Interspecimen comparison of the refractive index of fused silica. J. Opt. Soc. Am. 55, 1205–1209 (1965). https://doi.org/10.1364/JOSA.55.001205

24. M. Born, E. Wolf, Principles of Optics, 7th edn. (Cambridge University Press, Cambridge, 1999), Sect. 8.5.2

25. F. Olivier, A. Daami, C. Licitra, F. Templier, Shockley-Read-Hall and Auger non-radiative recombination in GaN based LEDs: a size effect study. Appl. Phys. Lett. 111, 022104 (2017). https://doi.org/10.1063/1.4993741

26. J.M. Smith, R. Ley, M.S. Wong, Y.H. Baek, J.H. Kang, C.H. Kim, M.J. Gordon, S. Nakamura, J.S. Speck, S.P. DenBaars, Comparison of size-dependent characteristics of blue and green InGaN microLEDs down to 1 μm in diameter. Appl. Phys. Lett. 116, 071102 (2020). https://doi.org/10.1063/1.5144819

27. M.S. Wong, D. Hwang, A.I. Alhassan, C. Lee, R. Ley, S. Nakamura, S.P. DenBaars, High efficiency of III-nitride micro-light-emitting diodes by sidewall passivation using atomic layer deposition. Opt. Express 26, 21324–21331 (2018). https://doi.org/10.1364/OE.26.021324